

MAGNETAR-POWERED SUPERNOVAE IN TWO DIMENSIONS. I. SUPERLUMINOUS SUPERNOVAE

KE-JUNG CHEN^{1,2,3}, S. E. WOOSLEY³, AND TUGULDUR SUKHBOLD³

Draft version November 9, 2018

ABSTRACT

Previous studies have shown that the radiation emitted by a rapidly rotating magnetar embedded in a young supernova can greatly amplify its luminosity. These one-dimensional studies have also revealed the existence of an instability arising from the piling up of radiatively accelerated matter in a thin dense shell deep inside the supernova. Here we examine the problem in two dimensions and find that, while instabilities cause mixing and fracture this shell into filamentary structures that reduce the density contrast, the concentration of matter in a hollow shell persists. The extent of the mixing depends upon the relative energy input by the magnetar and the kinetic energy of the inner ejecta. The light curve and spectrum of the resulting supernova will be appreciably altered, as will the appearance of the supernova remnant, which will be shellular and filamentary. A similar pile up and mixing might characterize other events where energy is input over an extended period by a centrally concentrated source, e.g. a pulsar, radioactive decay, a neutrino-powered wind, or colliding shells. The relevance of our models to the recent luminous transient ASASSN-15lh is briefly discussed.

Subject headings: stars:supernovae: general, magnetars, winds, outflows; physical data and processes: hydrodynamics, instabilities, shock waves

1. INTRODUCTION

Magnetars are neutron stars with unusually strong magnetic fields, typically greater than 10^{13} Gauss (G). Observational evidence suggests that magnetars form in a significant fraction of supernovae (Kouveliotou et al. 1998), where the strong magnetic field may be a consequence of the collapse of a rapidly differentially rotating iron core (Duncan & Thompson 1992; Thompson & Duncan 1993; Wheeler et al. 2000; Thompson et al. 2004; Mösta et al. 2015). It would thus not be surprising if magnetars are also frequently born with rapid rotation rates which they dissipate shortly after being born. Indeed, the so called “millisecond magnetar” is a popular model for the production of long-soft gamma-ray bursts (e.g. Metzger et al. 2011, 2015). Mazzali et al. (2014) and Cano et al. (2015) have pointed out that the upper bound of 2×10^{52} erg commonly assumed for the most rapidly rotating neutron stars may be reflected in an upper bound for the observed energy in supernovae accompanying GRBs. There the required field strength approaches 10^{16} G and the rotational energy is about 2×10^{52} erg or 20 Bethe (B), a substantial fraction of which is emitted in 10 sec. For less extreme field strengths in the range 10^{14} - 10^{15} G and rotation periods ~ 5 ms, the assumption of pulsar-like emission implies that a smaller amount of energy is emitted over a much longer time. Following a suggestion by Maeda et al. (2007), studies by Woosley (2010) and Kasen & Bildsten (2010) showed that supernovae containing moderately energetic magnetars can power exceptionally luminous transients sometimes referred to as superluminous

supernovae (e.g. Quimby et al. 2011; Gal-Yam 2012; In-serra et al. 2013, SLSNe). There, because of its late time introduction, a substantial fraction of the total rotational energy of the neutron star is emitted as light.

These same studies also revealed a shortcoming in the one-dimensional models. Since the rapidly rotating magnetar deposits an energy comparable to the kinetic energy of the slower moving ejecta of the original supernova, the deposition has consequences not only for the brightness of the supernova, but for its dynamics as well. The magnetar’s energy, presumably initially in the form of x-rays or gamma-rays and a wind, originates in a small volume. As a small amount of matter carries a large amount of energy outwards, it “snowplows” into the overlying ejecta. In 1D studies, this causes a pile up of most of the accelerated matter in a very thin shell. Eventually, the density contrast between this shell and its surroundings, which can approach a factor of 1,000 or more, causes numerical difficulty in the simulation. If real, this pile up of most of the ejecta into a thin shell would have consequences for the light curve and spectrum. Radiation would be unrealistically trapped, at least initially, inside the bubble it inflates, and the spectrum would show a large amount of matter moving at just one speed. This is not a realistic outcome.

Studies by Chevalier (1982); Jun (1998); Blondin et al. (2001) have shown that similar thin shells, formed by a pulsar wind in a supernova remnant, are unstable. A similar instability might be expected to lead to the break up of the shells in supernovae that magnetars accelerate. Ideally, 3D radiation-hydrodynamical simulations that well resolve both the energy deposition region of the pulsar and the unstable thin shell would be used to study this mixing and to obtain their light curves and spectra. Such simulations are beyond the present capability of our numerical codes and computational resources. As a first step, we have carried out 2D hydrodynamical simulations using a realistic magnetar progenitor, but neglecting ra-

¹ Division of Theoretical Astronomy, National Astronomical Observatory of Japan, Tokyo 181-8588, Japan

² Institute of Astronomy and Astrophysics, Academia Sinica, Taipei 10617, Taiwan

³ Department of Astronomy & Astrophysics, University of California, Santa Cruz, CA 95064, USA

* EACOA Fellow, email: ken.chen@nao.ac.jp

diation transport. The neglect of radiation transport is a reasonable approximation to the actual situation since the density spike forms at an early phase when the matter is still very optically thick and the radiation is strongly coupled with the gas flow.

The supernova models studied here start from a $6 M_{\odot}$ carbon-oxygen (CO) core that has been previously evolved to the presupernova stage (Sukhbold & Woosley 2014). The star’s $1.45 M_{\odot}$ iron-core is assumed to collapse to a magnetar. All external matter is ejected using a piston so as to provide a final kinetic energy of 1.2 B. The source of this initial explosion is unspecified, but could be either neutrino transport or the action of a rapidly rotating magnetized proto-neutron star itself. Any initial jet formation is neglected.

Two different magnetars are then embedded in these standard ejecta, both with a constant magnetic field strength of 4×10^{14} G, but having rotational energies either appreciably greater than or less than the initial (1.2 B) explosion energy. The magnetar is assumed to add power to the ejecta through its dipole emission. Its energy is deposited in a small region, along within small amount of matter to prevent the complete evacuation of the region that would result in it becoming optically thin. At too low a density, the energy deposited would also result in super-luminal motion since our code is not relativistic.

The structure of the paper is as follows; in Section 2, the progenitor model and the setup for the 2D simulations are described. In Section 3 and 4, the results of the 2D simulations are given, and the mechanics behind the formation of fluid instabilities discussed. We conclude in Section 5 and discuss the relevance of our 2D model for the extreme case of a 1 ms magnetar embedded in a $6 M_{\odot}$ core. This might be relevant to the recently discovered transient, SLSN candidate, ASASSN-15lh (Dong et al. 2015), if it is a magnetar-powered supernova. Some recent studies (Metzger & Stone 2015; Holoien et al. 2016, e.g.) have suggested that ASASSN-15lh might be a “tidal-disruption event” (TDE) instead of a supernova, but the actual situation is unclear at this time.

2. NUMERICAL METHOD

2.1. Presupernova Star

The progenitor is a $6 M_{\odot}$ CO star with an initial mass fractions of $^{12}\text{C}=0.14$ and $^{16}\text{O} = 0.86$, as might result from the evolution of a non-rotating solar metallicity star with a zero-age main sequence mass of $\sim 24 M_{\odot}$. This model, previously published by Sukhbold & Woosley (2014), has been followed, using the KEPLER code, through carbon, neon, oxygen and silicon burning and iron core collapse. It is presumed to have lost all its envelope and part of its helium core to a wind or a binary companion. A bare CO core was employed both for its simplicity of modeling on a 2D Eulerian grid and because many SLSNe have been observed to be Type I. If the star were a red or blue supergiant (RSG or BSG), there would be additional mixing when the fractured CO core ran into its low density hydrogen envelope.

The evolution of the CO core was followed until the collapse speed in its iron core ($1.45 M_{\odot}$) exceeded $1,000 \text{ km s}^{-1}$. The iron core was then replaced with a gravitational

point source and a parametrized piston that moved so as to eject all matter external to the iron core with a final kinetic energy, at infinity, without magnetar energy deposition, of 1.2 B. The explosion synthesized and ejected $0.22 M_{\odot}$ of ^{56}Ni . The structure of the ejecta 100 s after the launches a shock wave is shown in Fig. 1. At this time the original supernova shock has already exited the star and the supernova is coasting nearly homologously. The final velocity profile is very similar to that shown in the figure.

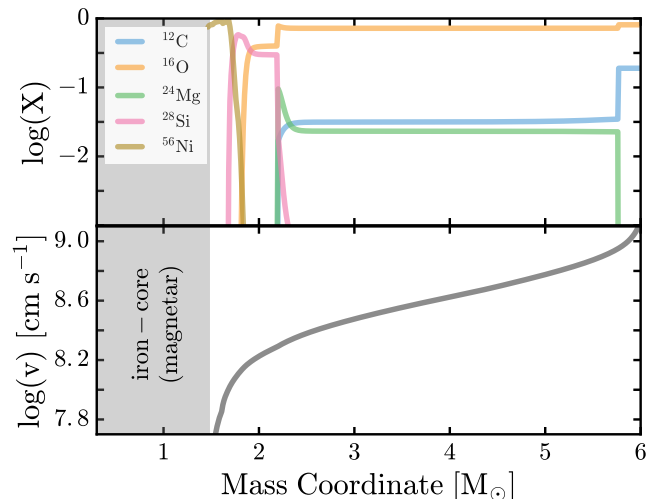


FIG. 1.— The starting model is a $6 M_{\odot}$ CO core evolved to the presupernova stage by Sukhbold & Woosley (2014). The iron core mass is $1.45 M_{\odot}$ (shaded gray). This core is assumed to collapse to a magnetar and eject all matter outside with a final kinetic energy of 1.2 B. The mass fractions of selected isotopes (top) and the velocity profile (bottom) in the ejecta are shown prior to any energy deposition by the magnetar. The velocity structure shown is that of the supernova 100 s after core collapse at which point the initial shock wave has already passed through the surface of the presupernova star. The final velocity profile is nearly identical. $0.17 M_{\odot}$ is ejected faster than $1 \times 10^9 \text{ cm s}^{-1}$ and $0.0027 M_{\odot}$, faster than $2 \times 10^9 \text{ cm s}^{-1}$.

2.2. Magnetar Input

Starting 100 s after the initial explosion, a simulated magnetar power source was introduced in the deep interior of the expanding ejecta with a luminosity given by the Larmor formula (Lyne & Graham-Smith 1990),

$$L_m = -\frac{32\pi^4}{3c^2} (BR_{\text{ns}}^3 \sin \alpha)^2 P^{-4} \quad (1)$$

$$\approx -1.0 \times 10^{49} B_{15}^2 P_{\text{ms}}^{-4} \text{ erg s}^{-1},$$

where the surface dipole field strength, $B_{15} = B/10^{15} \text{ G}$ is measured at the equator and the initial magnetar spin period P_{ms} is expressed in milliseconds. The radius of the neutron star is assumed to be $R_{\text{ns}} = 10^6 \text{ cm}$, and α is the inclination angle between the magnetic and rotational axes, taken $\alpha = 30^\circ$. Similar to Woosley (2010), the moment of inertia for the neutron star is taken to be $I = 10^{45} \text{ g cm}^2$, thus the rotational kinetic energy is:

$$E = \frac{1}{2} I \omega^2 \approx 2 \times 10^{52} P_{\text{ms}}^{-2} \text{ erg}. \quad (2)$$

It is common practice to take a limit of about 20 B

and one millisecond for the maximally rotating magnetar, though Metzger et al. (2015) have suggested a maximal value of 100 B in extreme cases. Assuming a constant magnetic field, eq. (1) and eq. (2) imply that the magnetar period, luminosity and energy evolution are given by

$$\begin{aligned} P(t) &\approx (1 + t/t_m)^{1/2} P_0 \text{ ms}, \\ L(t) &\approx (1 + t/t_m)^{-2} E_0 t_m^{-1} \text{ erg s}^{-1}, \\ E(t) &\approx (1 + t/t_m)^{-1} E_0 \text{ erg}, \end{aligned} \quad (3)$$

where $P_0 = P_{\text{ms}}(0)$, $E_0 = E(P_0)$ and $t_m \approx 2 \times 10^3 P_{\text{ms}}^2 B_{15}^{-2}$ is the magnetar spin-down timescale. In the 1D KEPLER calculations, the magnetar energy generation is spread uniformly through the inner ten Lagrangian zones of total mass $\sim 2.4 \times 10^{32}$ gm, with an approximately constant energy generation rate per gram. In the 2D Eulerian grid calculations, the power is deposited in a constant volume bounded by a radius of about 5×10^9 cm (1 ms run) and 5×10^{11} cm (5 ms run), both corresponding to 2 – 3% of the initial radius of ejecta at the time the calculation began. Both volumes are fixed and resolved in the 2D study by about 100 grid points and the short Courant time step in this small volume restricted the time scale of the calculation. Although CASTRO sub-cycles in time step for refined zones, the simulations still required numerous steps to evolve and that made them computationally expensive.

The evolution of the magnetar luminosity for a range of B-fields and two initial rotational rates is shown in Fig. 2. The energy deposition history is shown in black.

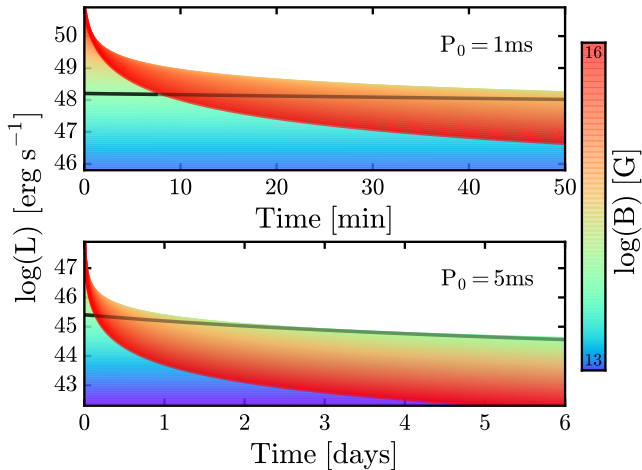


FIG. 2.— Energy deposition (eq. 3) due to a 1 ms magnetar (top) and a 5 ms magnetar (bottom). Color coding indicates a range of possibilities depending upon the magnetic field strength which varies in the plot from 10^{13} to 10^{16} G. The black lines correspond to a field strength of 4×10^{14} G as was used in this paper and the time range corresponds to the duration of the 2D studies in § 3.

2.3. 2D CASTRO Setup

CASTRO is a multi-dimensional adaptive-mesh-refinement (AMR) hydrodynamics code (Almgren et al. 2010; Zhang et al. 2011). It uses an unsplit piecewise-parabolic method (PPM) hydro scheme (Colella &

Woodward 1984) with multi-species advection and employs the Helmholtz equation of state (Timmes & Swesty 2000), which includes electron and positron pairs of arbitrary relativity and degeneracy, as well as ions, and radiation. Since the density of the supernova ejecta is low $< 10^7 \text{ g cm}^{-3}$, Coulomb corrections to the equation of state were neglected.

In both the KEPLER (1D) calculation and the CASTRO (2D) simulation, the effect of the magnetar was introduced 100 seconds after the initial explosion. By this time, all the piston energy has been deposited and the supernova has almost reached a coasting configuration. During the neglected 100 seconds, the fiducial magnetar with field strength 4×10^{14} G would have deposited only 0.6% of its total rotational energy for the 1 ms case, and 0.032% for the 5 ms case. This is small compared with either the total rotational energy or initial explosion energy. If the magnetar played a role in launching the explosion it must have had a larger field strength at that time and used physics not encapsulated in the simple dipole formula. The time chosen for linking from KEPLER to CASTRO was well before the development of any density spike in the KEPLER run, but after all nuclear burning had ceased. The 1D KEPLER profiles of density, velocity, temperature, and composition are mapped onto the 2D cylindrical grid of CASTRO, using the scheme of Chen et al. (2013), which conservatively maps mass, momentum, energy, isotope compositions from 1D profiles onto multi-dimensional grids.

The CASTRO simulation carried only an octant of the star. The computational domain was about 10 – 60 times the radius of the initial expanding ejecta. As is necessary for Eulerian codes, an artificial circumstellar medium (CSM) was included in the calculation. This medium had a density profile $\rho = \rho_0 (r/r_0)^{-3.1}$ where ρ_0 is the density at the radius of the initial expanding ejecta, r_0 . In the 1 ms model ρ_0 and r_0 were $2.11 \times 10^{-3} \text{ g cm}^{-3}$ and 1.75×10^{11} cm, respectively. In the 5 ms model they were $5.31 \times 10^{-9} \text{ g cm}^{-3}$ and 1.54×10^{13} cm. The CSM densities were extended from the edge of expanding SN ejecta and are much greater than would be characteristic of any reasonable pre-explosive mass loss rate. They are more like what might have existed had the core been inside of a supergiant star. For WR stars with $\dot{M} = 10^{-4} M_\odot \text{ yr}^{-1}$ and escape velocity $1 \times 10^8 \text{ cm s}^{-1}$, the CSM density at 10^{12} cm would be $\rho = 5 \times 10^{-12} \text{ g cm}^{-3}$. In the entire simulation domain, the total mass of this artificial medium was $0.15 M_\odot$ for the 1 ms run and $0.37 M_\odot$ for the 5 ms run. This CSM was used solely to maintain computational stability. The density falls off rapidly above the edge of the presupernova star. If the shock wave generated by magnetar energy deposition passed through a region where the density fell off more slowly than r^{-3} , a reverse shock would develop. This medium was constructed to decline rapidly enough in density to avoid this happening. There are such regions in the envelopes of both blue and red supergiants (e.g. Woosley & Weaver 1995; Herant & Woosley 1994) and including such envelopes would result in more mixing and fallback than calculated here (Joggerst et al. 2010; Chen et al. 2014a).

The CASTRO grid, at its coarsest level, had 256×256 zones. Six levels of adaptive mesh refinement were em-

ployed for an additional resolution of up to 64 (2^6). This degree of refinement was necessary to spatially resolve the energy deposition region, as well as the emergent fluid instabilities. This level of AMR implied an effective resolution of $16, 384 \times 16, 384$. The grid refinement criteria were based on gradients of density, velocity, and pressure. The hierarchy nested grids were also constructed in such a way that the energy deposition region near the magnetar was well resolved. Reflecting and outflow boundary conditions were set on the inner and outer boundaries in both r and z , respectively. A monopole approximation for self-gravity was included in which a 1D profile of gravitational force was constructed from the radial average of the density, then the gravitational field stress of each grid was calculated by the linear interpolation of the 1D profile. A point-like gravitational source of $1.45 M_{\odot}$ represented the magnetar.

When the 2D simulation began, 100 s after the initial core collapse, the initial shock from the 1.2 B explosion had already exited the surface of the star at $r \approx 2 \times 10^{11}$ cm and the entire star had nearly reached its terminal velocity (Fig. 1). A magnetar was then introduced with a power described by Eg.1 and Eg.3. Unlike the KEPLER run which deposited the energy at a constant rate per unit mass, since CASTRO uses an Eulerian grid, the energy deposition for the 2D models was a constant *per unit volume*. The mass of the 10 zones into which energy is deposited in the KEPLER run was $0.12 M_{\odot}$. In the 2D CASTRO simulations, the power is deposited in a constant volume bounded by a radius of about corresponding to 2% of the initial radius of ejecta.. In no case was the instantaneous kinetic energy in this material an appreciable fraction of the supernova explosion energy, i.e., most of the energy deposited went into doing work where the wind terminated.

3. RESULTS

Two sets of calculations were carried out, each using both KEPLER and CASTRO to model a given explosion in 1D and 2D. In both cases, a constant magnetar field strength of 4×10^{14} G was assumed, but the studies used initial rotational periods of 1 ms and 5 ms, corresponding to initial rotational energies of 20 B and 0.8 B respectively. Ideally, we would have liked to run both simulations for at least one magnetar spin-down time scale, t_m , which is 12,500 s and 312,000 s for the 1 ms and 5 ms cases respectively. Both KEPLER calculations were run to about 300 days and satisfied this condition. In 2D however, owing to the small timesteps in the finest zones ($\sim 10^{-3}$ s for the 1 ms run and $\sim 10^{-1}$ s for the 5 ms run), we were only able to simulate the first 3,000 s (50 min) of the 1 ms case and the first 520,000 s (6 days) of the 5 ms case. During these times 4.8 B out of the available 20 B is deposited in the high energy run and 0.5 B of the available 0.8 B deposited for the low energy run. Energy deposition in the high energy case was therefore far from over when the calculation was stopped, while the low energy case was essentially complete. These two cases were selected to represent situations where the deposited energy greatly exceeded or was substantially less than the initial dialed in supernova energy, 1.2B and the qualitative results will not be altered by this inadequacy. One should keep in mind though that the high energy model would have mixed even more than calculated here.

A recently discovered transient, ASASSN-15lh is possibly explained by a magnetar of rotational energy ≈ 40 B (Metzger et al. 2015; Bersten et al. 2016; Sukhbold & Woosley 2016), which resembles the 1 ms run here.

3.1. One-Dimensional Results

The bolometric light curves calculated using KEPLER are shown in Fig. 3. The 1 ms model produces a light curve that agrees well with the observations of the transient PTF10cwr (Quimby et al. 2011), while the 5 ms model roughly fits the measurements for the transient PTF11rks (Inserra et al. 2013). We do not include the ASASSN-15lh light curve here. Because Sukhbold & Woosley (2016) have given a light curve calculated for ASASSN-15lh by using KEPLER, and we are also waiting to see if the identification of this object as a supernova persists.

A density spike emerges in both calculations beginning ≈ 100 sec after the magnetar is turned on in the 1 ms model run and after $\approx 10,000$ sec in the 5 ms run. The amplitude of this spike grows with time and eventually includes most of the ejected mass. The density spike in the 1 ms model, shown in Fig. 4, grows to have a contrast of over three orders of magnitude with surrounding ejecta during the first 1,000 seconds. The density spike in the 5 ms model has a similar evolution, but grows on a longer time scale of hours. In past multi-dimensional simulations, similar spikes have been the location of fluid instabilities (e.g. Chevalier & Fransson 1992; Jun 1998; Blondin et al. 2001).

3.2. Two-Dimensional Results

The CASTRO calculations were begun from the KEPLER 1D model at ≈ 100 sec for the 1 ms run and $\approx 10,000$ sec for the 5 ms run. By this time, the original expanding ejecta had reached a radius of 1.75×10^{11} cm and $\sim 1.54 \times 10^{13}$ cm, respectively. The simulated domain used $r = 2.5 \times 10^{12}$ cm for the 1 ms model, and $r = 1 \times 10^{15}$ cm for the 5 ms model, with the finest zones being about 1.2×10^8 cm, and 6.1×10^{10} cm. The size of the domain determined the duration of the simulation. The difference in assumed magnetar rotation rates results in different energy deposition rates that cause the emerging spike to appear at very different times. For the 1 ms model, a much faster and more vigorous interaction with the overlying ejecta was observed. The 5 ms model had to be evolved much longer since the energy was deposited over a longer time. Although these were only 2D simulations, small time steps required by the fine spatial resolution still made them very computationally expensive. The 1 ms model took about 360,000 CPU hours on *Hopper* and the 5 ms model took 280,000 CPU hours on *Edison* at the National Energy Research Scientific Computing Center (NERSC).

3.2.1. Formation of a 2D radiative bubble

The energy injected by the magnetar heats the surrounding gas, causing it to expand and reach high speed. If the mass of the energy deposition region in KEPLER or the size of the energy deposition region in CASTRO had been too small, super-luminal motion would have resulted. Mass was therefore added, along with the energy in the CASTRO calculation so as to allow a high velocity wind, but prevent expansion faster than the speed of

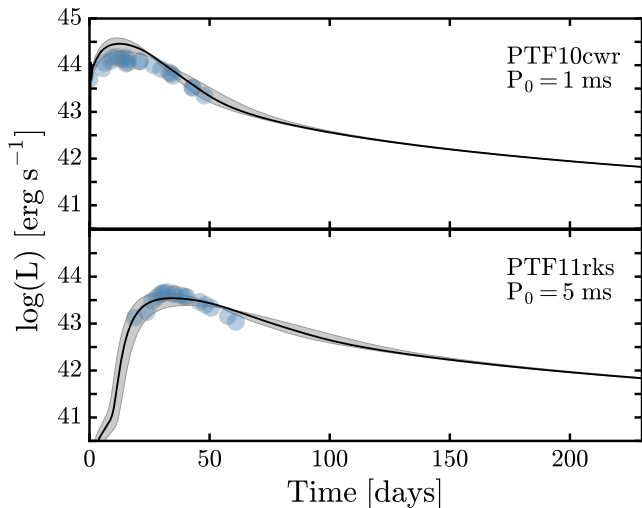


FIG. 3.— Bolometric light curves of PTF10cwr and PTF11rks (blue circles), compared with 1D model light curves calculated for the explosion shown in Fig. 1, but including an embedded magnetar with an initial rotational period of 1 ms or 5 ms, and a magnetic field strength of 4×10^{14} G. Both light curves were calculated in 1D using the KEPLER code and the results are sensitive to the assumed opacity. Gray ranges in both panels indicate choices of opacity $\kappa = 0.05 - 0.2 \text{ g cm}^{-2}$. The black curves assumed $\kappa = 0.1 \text{ g cm}^{-2}$.

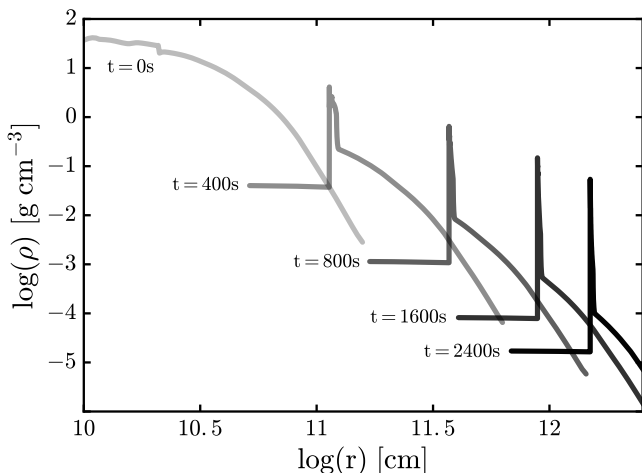


FIG. 4.— Early evolution of the density profiles from the 1 ms magnetar as calculated in 1D using the KEPLER code. Times are measured since the magnetar deposition was turned on, i.e., time since explosion minus 100 s. A prominent density spike starts to emerge at ≈ 100 s as the wind of the magnetar snowplows into overlying ejecta. The amplitude of the spike grows rapidly with time and eventually includes most of the ejected mass.

light. Had more mass been added, it would have moved with slower speed, but the work done at the wind termination shock, ρv^2 times the change in volume, would have been the same. The mass addition rates employed in CASTRO were $2.5 \times 10^{-6} M_{\odot} \text{ s}^{-1}$ for the 1 ms run and $1.2 \times 10^{-9} M_{\odot} \text{ s}^{-1}$ for the 5 ms run. During the entire run the accumulated mass was about $7.5 \times 10^{-3} M_{\odot}$ for the 1 ms run and $6.2 \times 10^{-4} M_{\odot}$ for the 5 ms run. Both values are negligible compared with the mass of the supernova ejecta.

In both the 1D and 2D calculations the gas energized by the magnetar pushes the overlying cooler material ahead of it and forms a dense shell. In 1D, there is no

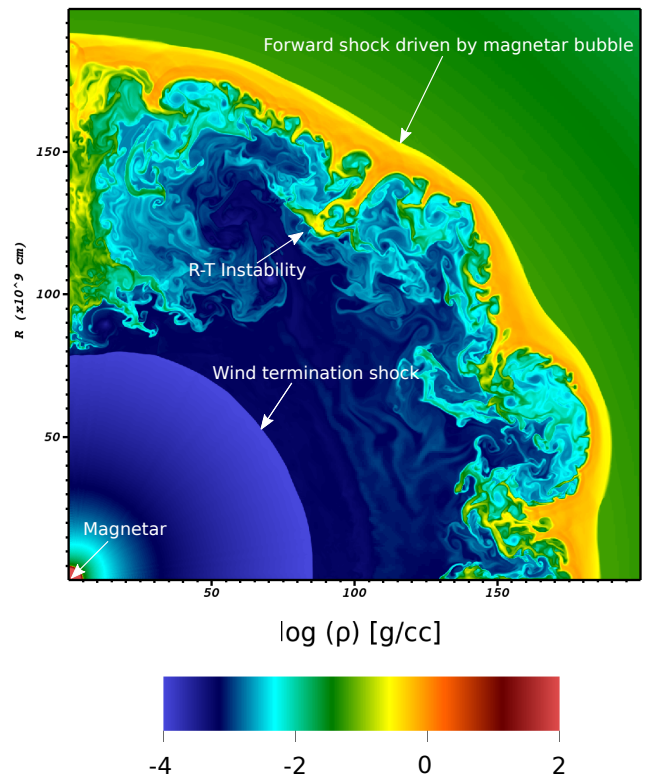


FIG. 5.— Density structure in the inner 2×10^{11} cm of the supernova for the 1 ms model at an early time in the 2D calculation. The time is 600 s after the magnetar was turned on and the boundary of the mixed region, also called the “radiation bubble”, extends to about 1.8×10^{11} cm. The boundary of smooth blue region inside 8.5×10^{10} cm marks the termination of the supersonic magnetar wind as it slams into the slower moving overlying ejecta. Later (e.g., Fig. 11), this termination shock becomes more irregular as the wind begins to break through. The ram pressure of the rapidly moving wind accelerates the overlying matter causing a pile up of density which increases roughly monotonically with radius between the wind termination shock and the forward shock. Accelerating this density inversion causes a Rayleigh-Taylor instability that mixes the region between the two shocks. This mixed region is not present in the 1D simulation (Fig. 4) where there is only one shock. Farther out, this mixture of radiation, wind, and supernova ejecta plows into slower moving supernova ejecta material resulting in a dense “pile-up” bounded by a second shock. The boundary of original supernova surface is at $\sim 1.1 \times 10^{12}$ cm, well outside the region plotted.

possibility for mixing so the shell is stable. The “termination shock” at the edge of the 10 Lagrangian shells where energy is deposited is located at almost the same radius as the “forward shock”, essentially the leading edge of the density pile up. There is effectively only one shock and all the swept up matter is compressed within it.

In 2D, however, the region inside the maximum density is unstable and mixes. A growing region develops between the wind termination shock and the forward shock where the acceleration caused by the wind operates in a region of decreasing density (Fig. 5). Near the forward shock and beyond there is no density inversion and no mixing, but behind it the ejecta is Rayleigh-Taylor unstable. The two shocks separate and between them the star is mixed and a convoluted density structure develops. We shall refer to the entire region of mixed matter and wind behind the forward shock as the “bubble”. For the 1 ms model, the bubble expands at the rate of $2 - 5 \times 10^8 \text{ cm s}^{-1}$, taking about 600 s to grow to the size

of the original progenitor star, $\approx 2 \times 10^{11}$ cm (Fig. 5). Later, for the 1 ms case, the bubble expands even faster, $> 10^9$ cm s $^{-1}$, and its leading edge starts to catch up with the outer edge of the original supernova.

Even though the ejected matter becomes mixed in 2D, it is still largely concentrated in the outer part of the bubble. The supernova is “hollow” and shellular with a thickness much less than its radius. So long as the energy being dumped in by the magnetar is comparable to the kinetic energy of the matter outside the bubble, the mixing and compression continue.

”Bubble breakout” is defined as the point when an appreciable part of the magnetar-accelerated shell first reaches a speed comparable to that of the fastest expanding ejecta. From Fig. 1, only $2.7 \times 10^{-3} M_{\odot}$ moves faster than 2×10^9 cm s $^{-1}$ in the original SN, so mixed material that attains that speed has clearly escaped. This is defined as the condition of “*strong breakout*”. A larger, but still small amount of ejecta, $0.17 M_{\odot}$, moves faster than 1×10^9 cm s $^{-1}$, and matching this speed defines “*weak breakout*”. More specifically, weak breakout occurs when a magnetar-accelerated shell mass of $0.17 M_{\odot}$ moves faster than 1×10^9 cm s $^{-1}$. Once this breakout occurs, the dense shell become fragmented and opens gaps that allow hot trapped magnetar wind, and eventually the magnetar radiation itself to escape. For the 1 ms case, this condition implied the full mixing of the entire explosion. The thick shell of bubble breaks though the original surface of the star as shown in Fig. 6(c) (d). About $1.89 M_{\odot}$ of the bubble has reached the weak breakout phase 2,400 sec after the explosion and more would continue had the calculation been run longer. The breakout of the bubble in the 5 ms model (Fig. 7) is less extreme. In this case, fragmentation and mixing is not as developed, but about $0.24 M_{\odot}$ of the bubble barely reaches weak breakout with a $25 - 30^{\circ}$ opening angle roughly 5 days after the explosion.

The dynamics of the breakout thus depends upon the relative energy input by the central magnetar and the original explosion. Breakout can happen, in principle, when the amount of energy deposited by the magnetar, $\int L_m dt$, and expended in doing PdV work at the termination shock, becomes comparable with the original kinetic energy of the ejecta. This is an approximate condition though. Neither the original supernova nor the magnetar-accelerated bubble move at uniform speed. The original supernova has very high speed at its edge due to shock steepening at breakout (Fig. 1). The bubble has variable speeds at different angles and, at late times, is honeycombed by magnetar wind that has broken though the termination shock (Fig. 11).

Nevertheless, the calculations suggest a breakout time, t_b , of roughly E_{sn}/L_m , where E_{sn} is the kinetic energy of the original supernova and L_m is the magnetar luminosity. For the 1 ms case, this gives $1.2 \times 10^{51}/10^{48} \sim 1200$ s which is consistent with the results of the simulation. For the 5 ms run, the total energy deposited by the magnetar is 0.8 B which close to E_{sn} . Only a fraction of the shell experiences breakout. Once the shell starts to fragment, however, the piston doing the PdV work is less efficient. Gaps are opened for the hot gas to break out. For the 1 ms model at the post breakout phase $t \sim 2400$ sec, 69% of magnetar energy went to radiation and 31% to accelerating the ejecta. It is possible that the dipole radiation

of the magnetar may be able to escape through the holes formed by the bubble as it breaks out (see also Metzger et al. 2014, 2015), especially since the calculation followed only a fraction of the energy deposition. Such radiation breakout may be a common occurrence in energetic magnetar-powered supernovae suggested Kasen & Bildsten (2010). More calculations including radiation transport and a realistic spectrum for the magnetar should be done in two dimensions to better determine the observable consequences of breakout.

3.2.2. Evolution to the Coasting Phase

Once the bubble breaks out of the expanding supernova ejecta, it runs into the artificial circumstellar medium (CSM). The deformed structure continues evolving as the bubble expands, however. Significant mixing has occurred inside the bubble and broken its spherical symmetry.

For the 1 ms model shown in (d) of Fig. 6, weak breakout has occurred and strong breakout will follow shortly. After this time, the evolution of fluid instabilities slows down, but will still continue since only about 20% of magnetar energy has been deposited. An increasing fraction of the injected energy would presumably escape from the perforated shell with a spectrum that might eventually resemble that of the pulsar (Kasen & Bildsten 2010).

The angle-averaged profiles of density are shown in Fig. 8. Spikes seen in the 1D KEPLER models do not disappear in 2D, but are substantially eroded and broadened. Fluid instabilities in the 2D study result in a “noisy bump” when angle averaged, but in fact the shell is being broken up and mixed. The relative density constraint, $\delta\rho = \rho - \langle\rho\rangle/\rho$ is 10 to 100 within the mixing region rather than up to 10^3 as seen in the 1D study. In 1D models, most radiation is emitted from the density spike, which suggests the radiation may continue to come from the mixed region in the multidimensional models since that is where most of the matter is.

Due to the continuing injection of energy by the central magnetar, the structure continues to evolve. When the bubble expands to a large radius ($>$ ten times radius of initial expanding ejecta), the ejecta are still not expanding fully homogeneously since the internal energy of gas still exceeds 10% of its kinetic energy, but a filamentary structure of the ejecta has been determined (Fig. 9). The 1D angle-averaged abundances are shown in Fig. 10 for the 1 ms model. The major mixing occurred at region of fragmented dense shell and some fraction of ^{56}Ni appears at the outer edge of the fragmented shell. If such dredging up of ^{56}Ni indeed happens at an early phase of magnetar evolution, there is the possibility of early gamma-ray detection from the ^{56}Ni decay in the local or nearby galaxies. The ^{56}Ni would leave footprints on the magnetar-powered SN remnant and might resemble the iron observed on the outskirts of the Cas A SN remnant (Vink 2008).

3.3. Discussion

3.3.1. Model Results

The fluid instabilities of a magnetar-powered supernova are similar to those previously found for pulsar-wind nebulae (Chevalier & Fransson 1992; Jun 1998; Blondin et al. 2001). Two kinds of instabilities are seen. When

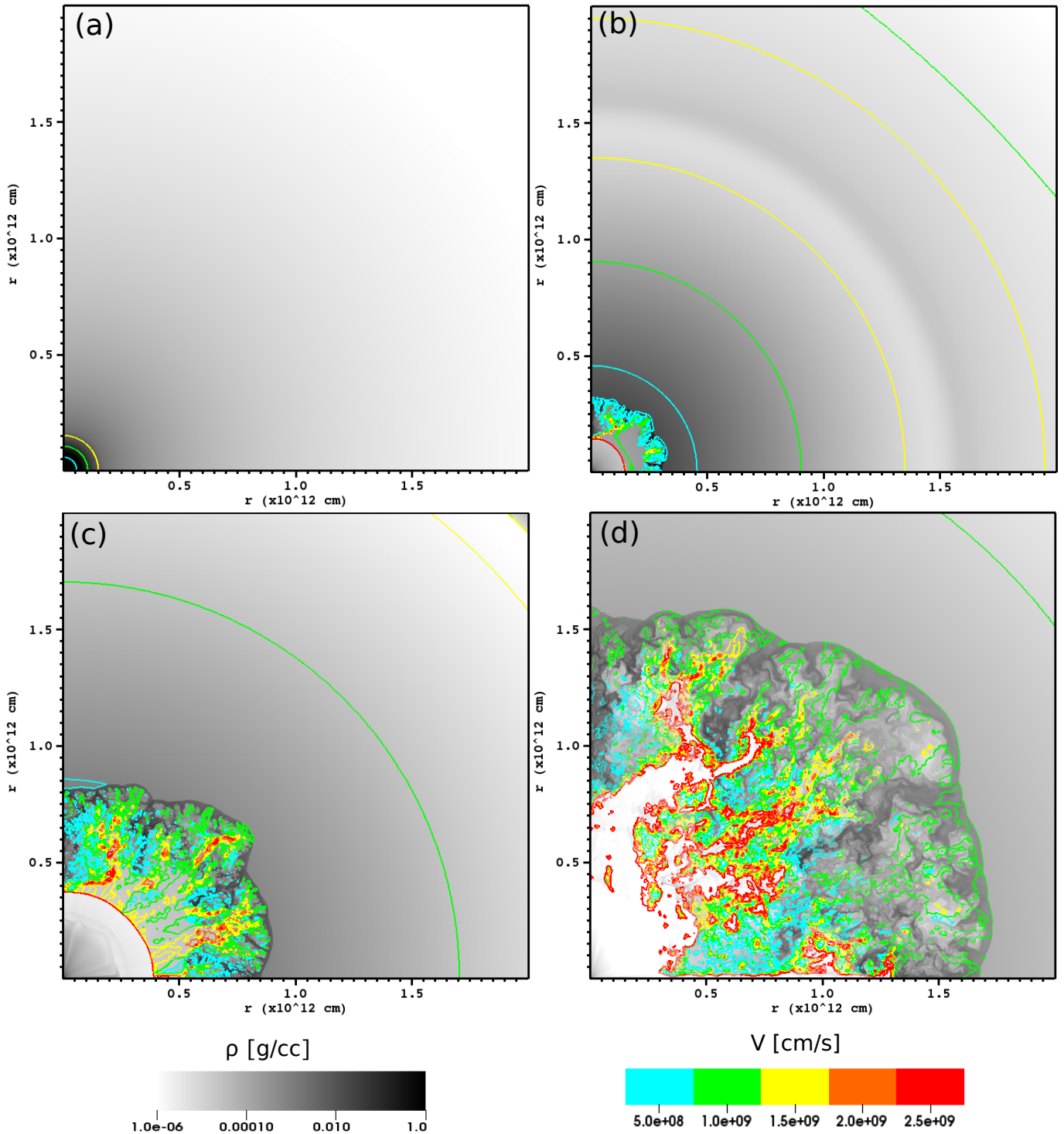


FIG. 6.— Evolution of the mixed region in the early phases of the 1 ms model. Color coding and contours show the densities and velocities of SN ejecta. Panels (a) - (d) are at 0, 800, 1,600, and 2,400 seconds, respectively. After the magnetar begins to deposit energy, fluid instabilities develop from tiny fingers as shown in Panel (b) and a thin shell has formed. The shell is promptly accelerated by the high-speed magnetar wind. In Panel (c), some fraction of shell and the gas behind it has exceeded 1×10^9 cm s $^{-1}$. In Panel (d), the entire shell has exceeded 1×10^9 cm s $^{-1}$ and the week breakout has occurred. It is expected that the strong breakout ($v \geq 2 \times 10^9$ cm s $^{-1}$) will occur shortly. Velocities in the low density region (white area) in Panel (d) have exceeded 10^{10} cm s $^{-1}$.

the magnetar first heats the gas and drives an outflow (the “magnetar wind”) an instability develops near the contact discontinuity where dense ejecta is being accelerated. The low density hot gas colliding with the dense ejecta is RT unstable Fig. 5. A number of long fingers are generated by this instability, and these fingers are Kelvin-Helmholtz unstable at their boundaries due to their relative motion with respect to the background flow.

As the shell approaches the boundary of the expanding ejecta, its expansion rate can be estimated using dimensional analysis (Jun 1998), $r \propto t^{(6-a-b)/(5-a)}$, where a and b are the power-law indices for the moving ejecta density ($\rho \propto r^{-a}$) and the magnetar luminosity ($L_m \propto t^{-b}$) respectively. Using the CSM density ($a = 3.1$) and assuming a constant magnetar luminosity ($b = 0$), the bubble radius expands roughly as $r \propto t^{1.52}$. The shell accelerates and expands supersonically as shown in Fig. 11. The second Rayleigh-Taylor instability is driven by the acceleration of bubble’s shell. This is the nonlinear thin shell instability (NTSI) found by Vishniac (1994)). It happens when a thin slab bounded by a shock on one side and a contact discontinuity to a higher temperature region on the other is subject to a nonlinear instability in which the perturbation’s wavelength is larger than the width of shell. In our case, the shell is bounded by the forward shock and relativistic magnetar wind. The NTSI provides a major mechanism to drive the mixing and fragmentation formation. The original motivation to setup $a = 3.1$ is to prevent the reverse shock formation so it would not induce additional mixing. In this study, a luminosity source is provided from the central magnetar. The forward shock of expanding bubble is no longer adiabatic. This shock indeed accelerates both in the constant density CSM ($a = 0$) and in wind-like ISM ($a = 2$). Since the growth of rate of NTSI is marginally proportional to the shell velocities (Blondin & Marks 1996). If we employ the constant CSM or wind-like ISM in our simulations, the overall fragmentation structure may not be as evolved as the results we present here.

In the Type I supernova model studied, radiation from sufficiently energetic magnetars breaks out of the dense layer bounding the radiative bubble during the NTSI phase and becomes observable. Depending upon the magnetar spectrum, this emission might take the form of hard x-rays. In addition, the mixing driven by the fluid instabilities alters the dynamics and chemical compositions of supernovae ejecta. Since mixing is strongest in the region of the flow from which most of the radiation originates, it will certainly affect the supernova light curve and spectrum. As shown in Fig. 12, it is possible that high speed iron can be observed in the outskirts of the SN remnant.

Our present simulations do not include radiation transport and the omission becomes increasingly unrealistic at late times when the cooling of the ejecta might affect its dynamics. The earlier fragmentation of ejecta in our simulations may seed the large-scale inhomogeneity at later times. The magnetar is also assumed here to have a constant dipole field strength while some decay would not be surprising.

3.3.2. Relevance to ASASSN-151h

Assuming that the bright transient ASASSN-151h was a supernova, which is still quite controversial (Brown 2015; Milisavljevic et al. 2015; Margutti 2015), it is the brightest supernova recorded to this date (Dong et al. 2015). One interpretation is a magnetar-illuminated explosion with a very high initial magnetar energy, 40 B and a relatively low magnetic field strength, $10^{13} - 10^{14}$ G embedded in a stripped core of 5 - 10 M_\odot (Metzger et al. 2015; Bersten et al. 2016; Dai et al. 2016; Sukhbold & Woosley 2016). We have shown here that mixing and breakout are sensitive to the magnetar energy. Mixing is maximal when the energy input by the magnetar greatly exceeds any other source driving the explosion, and the magnetar decay time scale is comparable to the expansion time scale for the star. In this regard, the proposed models for ASASSN-151h are similar to the 1 ms model calculated here and mixing and breakout should also be similar. Three signatures of the model are a strong density inversion inside a shell that contains most of the ejected mass; extensive mixing; and magnetar wind and radiation breakout. We have not calculated the time-dependent spectrum of our models, but our results suggest that the spectrum of a 2D model will differ appreciably from a 1D model. Mixing will result in composition inversions. The heavy elements will not mostly be in a shell traveling at a single speed, giving rise to “boxy”, “flat-topped” spectral lines (e.g. Höflich et al. 2004). The mixed heavy elements would have a high velocity dispersion as shown in Fig. 11 and magnetar radiation would also leak out earlier and the breakout transient predicted by Metzger et al. (2014) would have an earlier onset.

4. CONCLUSIONS

Previous 1D models for magnetar-powered supernovae could not properly model the fluid instabilities and mixing that necessarily occur when an energy that is not trivial compared with the kinetic energy of the ejecta is deposited in a small amount of deeply situated matter. They instead produced an unphysical density spike that is smeared over a broader range of radii and mixed in a more realistic 2D hydro simulation. The mixed region corresponds, approximately, to the mass of the inner ejecta that had an initial kinetic energy equal to the energy deposited by the magnetar. If the magnetar energy exceeds the initial kinetic energy of the entire supernova, breakout will occur on a time scale given by the time required to roughly double the supernova energy. After breakout, about 30% of the deposited energy in the models studied goes into further accelerating the ejecta. Most of the rest, i.e., that part not further adiabatically degraded, should appear as light. Assuming a canonical initial supernova energy (without magnetar input) of 1×10^{51} erg, instabilities and mixing will be a dominant feature when the initial magnetar period is less than 3 ms, but a less energetic magnetar or radioactivity could still appreciably alter the spectrum and supernova remnant morphology. The resulting mixing transform the supernova ejecta into filamentary structures whose morphology resembles the Crab Nebula. While our calculations did not include radiation transport, the filamentary structure found here may be even more enhanced by cooling or radiative RT instabilities (Krumholz et al. 2009; Jiang et al. 2013; Tsang & Milosavljević 2015).

In a case where the magnetar energy deposited was

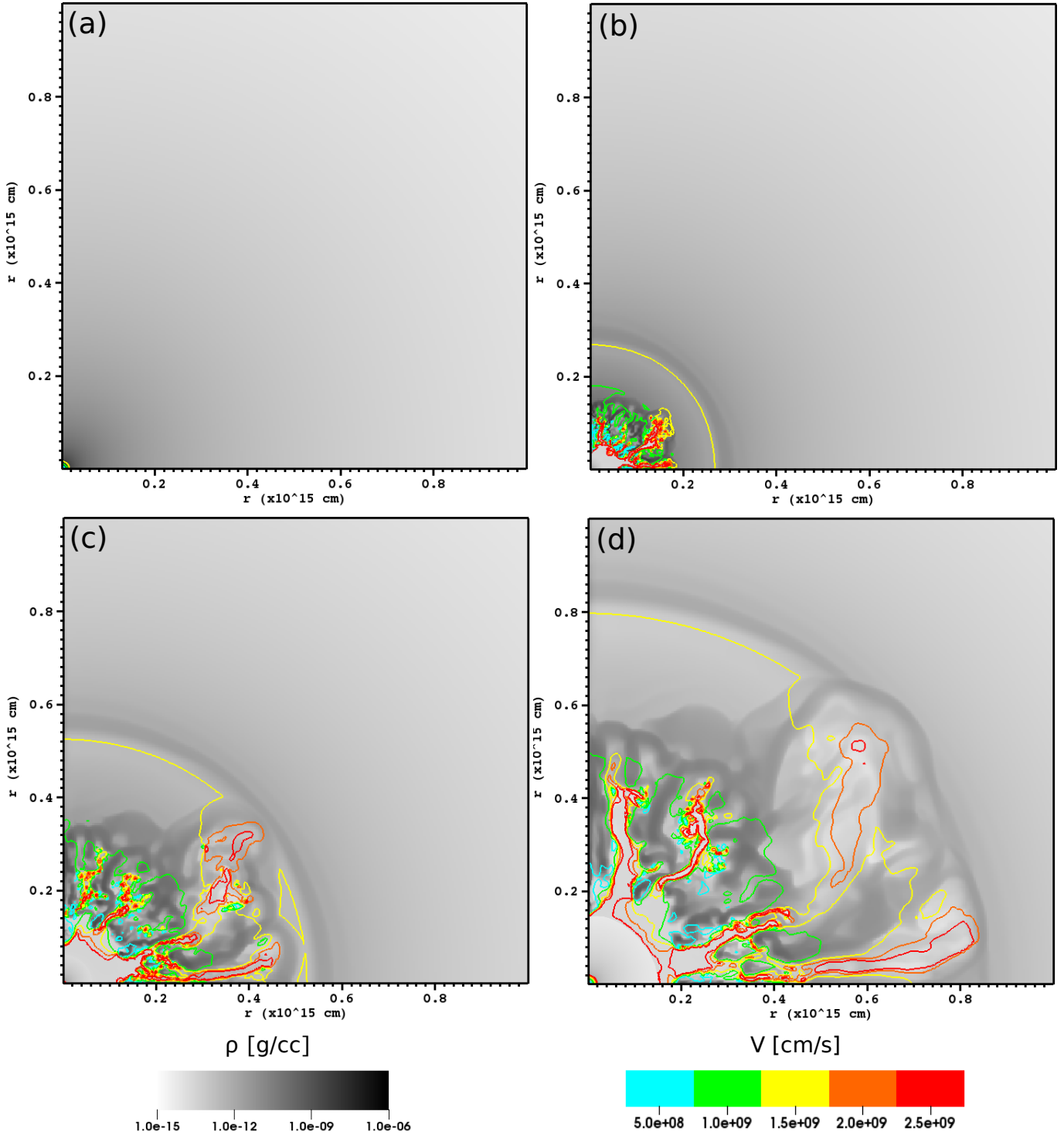


FIG. 7.— Similar to Fig. 6 but for the 5 ms model. Panels (a) - (d) now show the densities and velocities at 0, 2, 4, and 6 days, respectively. In Panel (b), fluid instabilities again appear and two prominent fingers have formed. The dense shell is eventually penetrated by these two fingers (Panel (d)). Only the dilute gas behind the shells exceeds 1×10^9 cm s $^{-1}$. The shell itself does not move faster because of the smaller energy deposited and most of the shell will not break out. The overall mixing and fragmentation is less extensive in comparison with the 1 ms model.

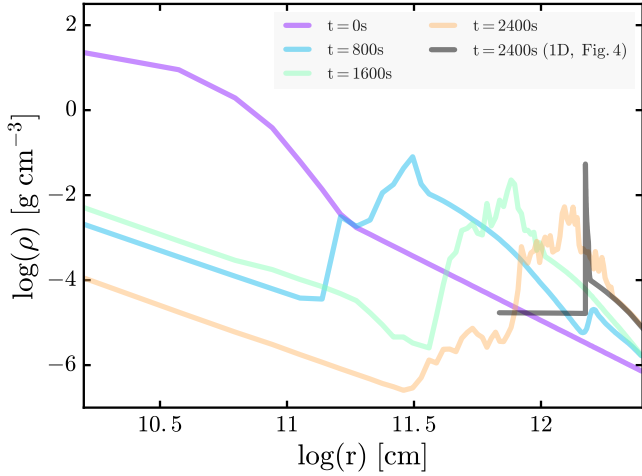


FIG. 8.— Angle-averaged density profiles of 1 ms case, as calculated in the 2D CASTRO model. Curves represent profile snapshots shown in Fig. 6. The fluid instabilities in 2D smear out the density spike seen in 1D and cause mixing. The profile from the 1D KEPLER run (black curve, Fig. 4) at 2400 s is also shown for comparison. Note that even in 2D the supernova is still “shellular” with a hollow center.

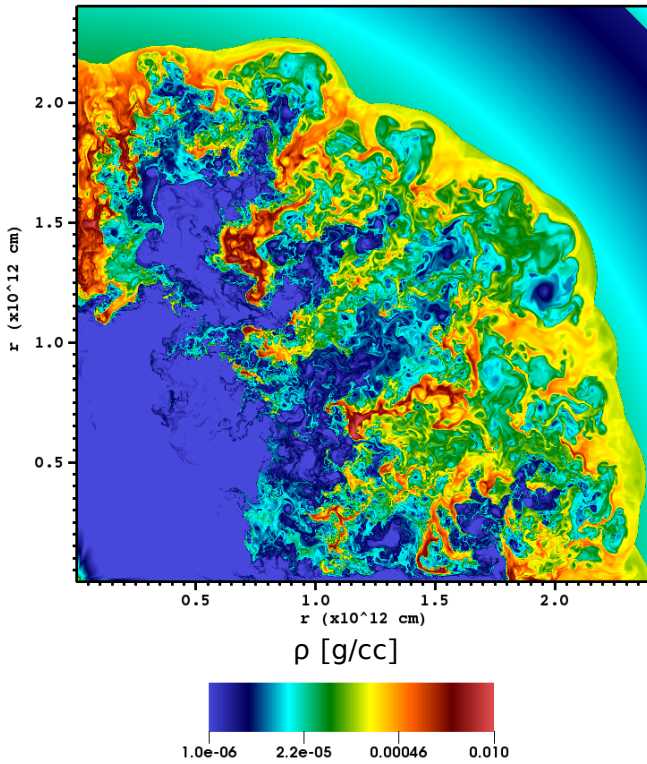


FIG. 9.— Mixing of the 1 ms model is shown for the last model calculated, $t \approx 3,000$ s. Density is given on a logarithmic scale from 10^{-6} g cm $^{-3}$ to 10^{-2} g cm $^{-3}$. Regions of low density are also regions of high expansion speed (Fig. 11). The highly fractured nature of the mixed ejecta will alter its observational signatures and the structure of the supernova remnant.

0.5 B (out of a total available 0.8 B) in a 1.2 B explosion, breakout was marginal. In a more energetic case where 4.8 B (out of an available 20 B) was deposited, the supernova was shattered and mixing was extensive. This mixing would have major implications for the color and spectrum of the supernova and for the morphology

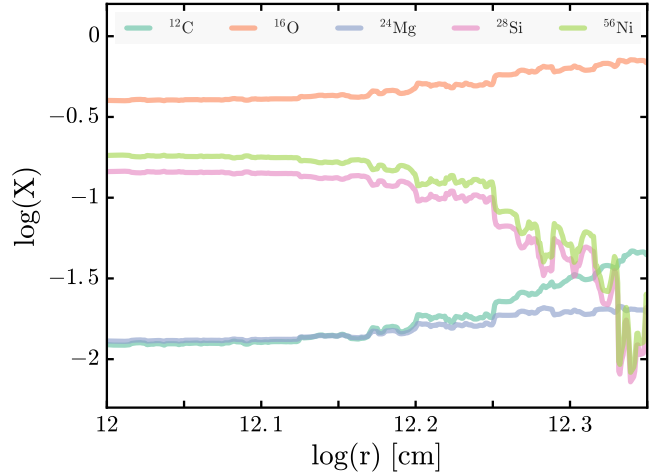


FIG. 10.— Angle-averaged elemental abundances for the 1 ms model at $t = 3,000$ s. Some ^{56}Ni from the interior of star has been mixed out and enriches the outskirts of the bubble with a mass fraction of about 0.01. This will leave a compositional imprint on the composition distribution in the supernova remnant.

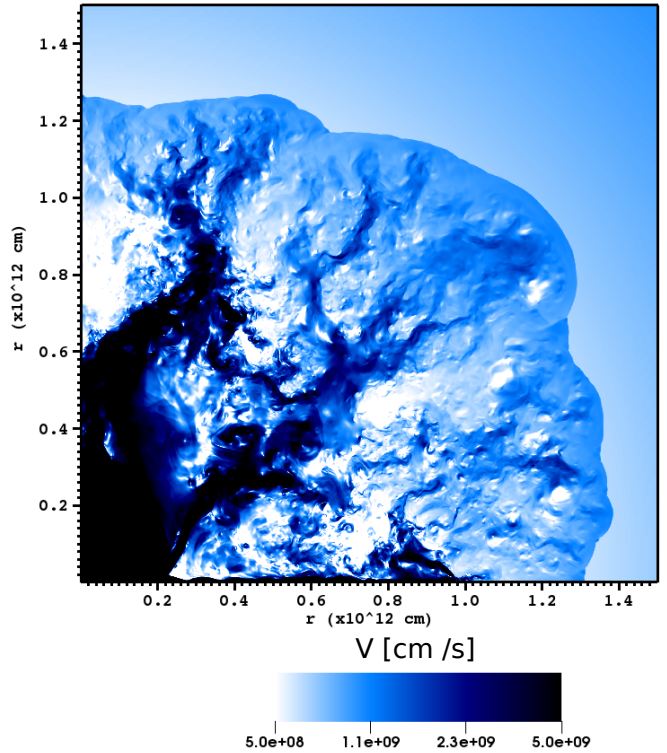


FIG. 11.— Ejecta velocity in the 1 ms model at $t \approx 2,000$ s, near weak breakout. The color scale indicates a logarithmic scale from 5×10^8 cm s $^{-1}$ to 5×10^9 cm s $^{-1}$. There is a clear interface between the bubble and its surroundings that marks the location of a shock front. Within the bubble, expansion speeds approach a fraction of light speed. Farther out, channels of high speed ejecta are opening up. At the time shown only 3.2 B of the available 20 B has deposited and the bubble will achieve strong breakout shortly.

of its remnant, and might be distinguishable from, e.g., circumstellar interaction (Chen et al. 2014b). One massive shell impacting another of comparable or lesser mass would probably lead to less mixing than exploding a star with a bubble of radiation.

The present calculations are for bare CO cores, chiefly

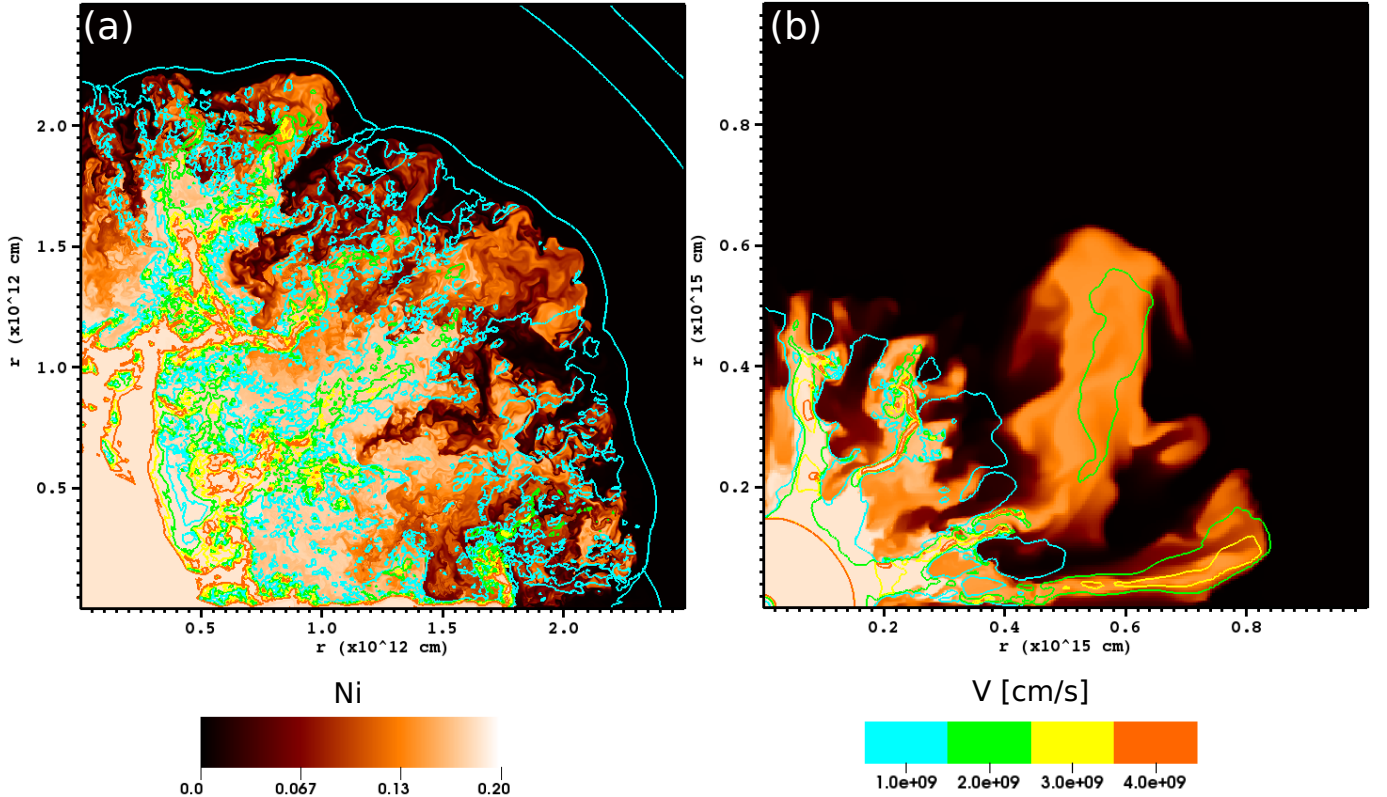


FIG. 12.— 2D ^{56}Ni and velocity distributions for the 1 ms model (Panel a) and 5 ms model (Panel b) at the last model calculated. ^{56}Ni is mixed out with velocities of $1 \times 10^9 \text{ cm s}^{-1}$. In Panel a, the entire shell has reached the weak breakout regime and will become optically thin region when the strong breakout occurs. In Panel b, two prominent ^{56}Ni fingers appear at the breakout phase. The mixing of ^{56}Ni and other chemical elements may be reflected in the spectrum.

as a matter of computational efficiency. A larger star would have required a larger grid, more levels of AMR, and taken longer to run. Many SLSNe are Type I, however, and stars with extended envelopes and mass loss may be more likely to brake their cores so that slower magnetar with weaker fields (Duncan & Thompson 1992), are produced (Heger et al. 2005; Woosley & Heger 2006). Were our cores to be embedded in low density red or blue supergiants, much more mixing and fragmentation is expected since the already clumpy ejecta would seed additional instabilities in the reverse shock. While there are many ways to mix a supernova, it could be that the extreme mixing in magnetar-powered supernovae is a diagnostic for their late time energy input.

The models calculated here should be generally characteristic of other situations in supernovae where the nonlinear thin shell instability (NTSI) plays an important role that is events where an enduring central energy source piles up matter in a dense shell. An off-center density maximum necessary has a region where the density decreases with radius and accelerating that inverted density will result in mixing. If the energy driving the compression is comparable kinetic energy of the dense shell, extensive mixing and fragmentation will occur. Other examples besides magnetar winds are the decay of radioactivity, neutrino-driven winds, and colliding shells. The energy from the decay of $0.1 M_{\odot}$ of ^{56}Ni and ^{56}Co will release $1.9 \times 10^{49} \text{ erg}$, which is comparable to the

kinetic energy in the inner $2 M_{\odot}$ of a typical $15 M_{\odot}$ supernova. Mixing is likely to occur in at least that volume.

The Crab Nebula, which many of our 2D figures qualitatively resemble, is believed to have been the low-energy explosion of a star near $10 M_{\odot}$ (e.g. Smith 2013) and to have had a low explosion energy (Yang & Chevalier 2015). This is consistent with an explosion powered in part, or wholly by a neutrino-powered wind (Arcones et al. 2007; Melson et al. 2015). The high velocity wind pushing on an essentially stationary star might be expected to develop the same instabilities studied here, albeit for just the first 10 seconds or so. These instabilities might provide the seeds for subsequent mixing in the magnetar wind.

Colliding shells, such as those produced in pulsational-pair instability supernovae, are also known to produce similar density spikes and 2D mixing like that studied here (Chen et al. 2014a). In future papers, we will use the radiation transport capabilities of the CASTRO code (Zhang et al. 2013) to better examine these explosions and provide more realistic observable diagnostics.

The authors are grateful to the anonymous referee for providing insightful comments. The authors thank Ann Almgren and Weiqun Zhang for help with the CASTRO code. We also thank Alexander Heger, Mark Krumholz, and Dan Kasen for useful discussions. K.C. acknowledges the support of EACOA Fellowship from the East

Asian Core Observatories Association and the hospitality of Aspen Center for Physics, which is supported by National Science Foundation grant PHY-1066293. Work at UCSC has been supported by an IAU-Gruber Fellowship, the DOE HEP Program (de-sc0010676) and the NASA Theory Program (NNX14AH34G). CASTRO was developed through the DOE SciDAC program by grants

DE-AC02-05CH11231, and DE-FC02-09ER41618. Numerical simulations are supported by the National Energy Research Scientific Computing Center (NERSC), and the Center for Computational Astrophysics (CfCA) at National Astronomical Observatory of Japan (NAOJ).

REFERENCES

- Almgren, A. S., Beckner, V. E., Bell, J. B., et al. 2010, *ApJ*, 715, 1221
- Arcones, A., Janka, H.-T., & Scheck, L. 2007, *A&A*, 467, 1227
- Bersten, M. C., Benvenuto, O. G., Orellana, M., & Nomoto, K. 2016, arXiv:1601.01021
- Blondin, J. M., & Marks, B. S. 1996, 1, 235
- Blondin, J. M., Chevalier, R. A., & Frierson, D. M. 2001, *ApJ*, 563, 806
- Brown, P. J. 2015, *The Astronomer's Telegram*, 8086,
- Cano, Z., de Ugarte Postigo, A., Perley, D., et al. 2015, *MNRAS*, 452, 1535
- Chandrasekhar, S. 1961, *International Series of Monographs on Physics*, Oxford: Clarendon, 1961,
- Chen, K.-J., Heger, A., & Almgren, A. S. 2013, *Astronomy and Computing*, 3, 70
- Chen, K.-J., Heger, A., Woosley, S., Almgren, A., & Whalen, D. J. 2014, *ApJ*, 792, 44
- Chen, K.-J., Woosley, S., Heger, A., Almgren, A., & Whalen, D. J. 2014, *ApJ*, 792, 28
- Chevalier, R. A. 1982, *ApJ*, 259, L85
- Chevalier, R. A., & Fransson, C. 1992, *ApJ*, 395, 540
- Colella, P., & Woodward, P. R. 1984, *Journal of Computational Physics*, 54, 174
- Dai, Z. G., Wang, S. Q., Wang, J. S., Wang, L. J., & Yu, Y. W. 2016, *ApJ*, 817, 132
- Dong, S., Shappee, B. J., Prieto, J. L., et al. 2015, arXiv:1507.03010
- Duncan, R. C., & Thompson, C. 1992, *ApJ*, 392, L9
- Gal-Yam, A. 2012, *Science*, 337, 927
- Heger, A., Woosley, S. E., & Spruit, H. C. 2005, *ApJ*, 626, 350
- Herant, M., & Woosley, S. E. 1994, *ApJ*, 425, 814
- Höflich, P., Gerardy, C. L., Nomoto, K., et al. 2004, *ApJ*, 617, 1258
- Holoien, T. W.-S., Kochanek, C. S., Prieto, J. L., et al. 2016, arXiv:1602.01088
- Inserra, C., Smartt, S. J., Jerkstrand, A., et al. 2013, *ApJ*, 770, 128
- Jiang, Y.-F., Davis, S. W., & Stone, J. M. 2013, *ApJ*, 763, 102
- Joggerst, C. C., Almgren, A., & Woosley, S. E. 2010, *ApJ*, 723, 353
- Jun, B.-I. 1998, *ApJ*, 499, 282
- Kasen, D., & Bildsten, L. 2010, *ApJ*, 717, 245
- Krumholz, M. R., Klein, R. I., McKee, C. F., Offner, S. S. R., & Cunningham, A. J. 2009, *Science*, 323, 754
- Kouveliotou, C., Dieters, S., Strohmayer, T., et al. 1998, *Nature*, 393, 235
- Lyne, A. G., & Graham-Smith, F. 1990, *Cambridge, England and New York, Cambridge University Press (Cambridge Astrophysics Series, No. 16)*, 1990, 285 p., 16,
- Maeda, K., Tanaka, M., Nomoto, K., et al. 2007, *ApJ*, 666, 1069
- Margutti, R. 2015, *The Astronomer's Telegram*, 8089,
- Mazzali, P. A., McFadyen, A. I., Woosley, S. E., Pian, E., & Tanaka, M. 2014, *MNRAS*, 443, 67
- Melson, T., Janka, H.-T., & Marek, A. 2015, *ApJ*, 801, L24
- Metzger, B. D., Giannios, D., Thompson, T. A., Bucciantini, N., & Quataert, E. 2011, *MNRAS*, 413, 2031
- Metzger, B. D., Vurm, I., Hascoët, R., & Beloborodov, A. M. 2014, *MNRAS*, 437, 703
- Metzger, B. D., Margalit, B., Kasen, D., & Quataert, E. 2015, *MNRAS*, 454, 3311
- Metzger, B. D., & Stone, N. C. 2015, arXiv:1506.03453
- Milisavljevic, D., James, D. J., Marshall, J. L., et al. 2015, *The Astronomer's Telegram*, 8216,
- Mösta, P., Ott, C. D., Radice, D., et al. 2015, *Nature*, 528, 376
- Quimby, R. M., Kulkarni, S. R., Kasliwal, M. M., et al. 2011, *Nature*, 474, 487
- Sedov, L. I. 1959, *Similarity and Dimensional Methods in Mechanics*, New York: Academic Press, 1959,
- Smith, N. 2013, *MNRAS*, 434, 102
- Sukhbold, T., & Woosley, S. E. 2014, *ApJ*, 783, 10
- Sukhbold, T., & Woosley, S. 2016, arXiv:1602.04865
- Tsang, B. T.-H., & Milosavljević, M. 2015, *MNRAS*, 453, 1108
- Timmes, F. X., & Swesty, F. D. 2000, *ApJS*, 126, 501
- Thompson, C., & Duncan, R. C. 1993, *ApJ*, 408, 194
- Thompson, T. A., Chang, P., & Quataert, E. 2004, *ApJ*, 611, 380
- Vishniac, E. T. 1994, *ApJ*, 428, 186
- Vink, J. 2008, *Advances in Space Research*, 41, 503
- Weaver, T. A., Zimmerman, G. B., & Woosley, S. E. 1978, *ApJ*, 225, 1021
- Wheeler, J. C., Yi, I., Höflich, P., & Wang, L. 2000, *ApJ*, 537, 810
- Woosley, S. E., & Weaver, T. A. 1995, *ApJS*, 101, 181
- Woosley, S. E., Heger, A., & Weaver, T. A. 2002, *Reviews of Modern Physics*, 74, 1015
- Woosley, S. E., & Heger, A. 2006, *ApJ*, 637, 914
- Woosley, S. E. 2010, *ApJ*, 719, L204
- Yang, H., & Chevalier, R. A. 2015, *ApJ*, 806, 153
- Zhang, W., Howell, L., Almgren, A., Burrows, A., & Bell, J. 2011, *ApJS*, 196, 20
- Zhang, W., Howell, L., Almgren, A., et al. 2013, *ApJS*, 204, 7